A Novel Multiple-Ring Aromatic Spacer Based 2D Ruddlesden–Popper CsPbI$_3$ Solar Cell with Record Efficiency Beyond 16%

Yao, Huanhuan; Li, Zhizai; Shi, Chang; Xu, Youkui; Wang, Qian; Li, Zhen Hua; Peng, Guoqiang; Lei, Yutian; Wang, Haoxu; More Authors

Important note
To cite this publication, please use the final published version (if applicable).
Please check the document version above.

A Novel Multiple-Ring Aromatic Spacer Based 2D Ruddlesden–Popper CsPbI₃ Solar Cell with Record Efficiency Beyond 16%

Huanhuan Yao, Zhizai Li, Chang Shi, Youkui Xu, Qian Wang, ZhenHua Li,* Guoqiang Peng, Yutian Lei, Haoxu Wang, Zhipeng Ci,* and Zhiwen Jin*

Two-dimensional (2D) Ruddlesden–Popper (RP) CsPbI₃ perovskite possesses superior phase stability by introducing steric hindrance. However, due to the quantum and dielectric confinement effect, 2D structures usually exhibit large exciton binding energy, and the charge tunneling barrier across the organic interlayer is difficult to eliminate, resulting in poor charge transport and performance. Here, a multiple-ring aromatic ammonium, 1-naphthylamine (1-NA) spacer is developed for 2D RP CsPbI₃ perovskite solar cell (PSC). Theoretical simulations and experimental characterizations demonstrate that the 2D RP CsPbI₃ perovskite using 1-NA spacer with extended π-conjugation lengths reduces the exciton binding energy and facilitates the efficient separation of excitons. In addition, its cations have a significant contribution to the conduction band, which can reduce the bandgap, promote electronic coupling between organic and inorganic layers, and improve interlayer charge transport. Importantly, the strong π–π conjugation of 1-NA spacer can enhance intermolecular interactions and hydrogen bonding, and prepare high-quality films with preferred vertical orientation, resulting in lower defect density, and directional charge transport. As a result, the $(1\text{-}NA)_2(Cs)_3Pb_4I_{13}$ PSC exhibits a record 16.62% performance with enhanced stability. This work provides an efficient approach to improve charge transport and device performance by developing multiple-ring aromatic spacers.

1. Introduction

Compared with the phase-transition-prone 3D CsPbI₃, 2D Ruddlesden–Popper (RP) CsPbI₃ materials have received extensive attention in recent years. This is attributed to the introduction

of hydrophobic organic cations at its component level not only improves the moisture resistance of the film and inhibits ion migration, but more importantly, it can also generate steric hindrance to prevent phase transitions and improve the environmental stability.[1–6] Despite improved stability, the best power conversion efficiency (PCE) of the reported 2D ($n = 5$) RP CsPbI₃ perovskite solar cells (PSCs) is only 16.00%, which still lags behind that of 3D CsPbI₃ PSCs (21.00%).[7,8] Therefore, further optimizing its performance is a problem that needs to be dealt with to meet the market demand of photovoltaic devices.

Through analysis, the main reason for limiting the performance of 2D RP CsPbI₃ PSCs is poor charge transport due to the choice of insulating cations used in the organic layer, specifically the following two points: 1) The reduced dimensionality of the material and the dielectric confinement attributed to the dielectric mismatch between the $[PbI_6]^{4-}$ octahedron and organic cation layers lead to 2D structure with large exciton binding energy up to several hundreds of meV, much larger than that of the 3D structure.[9–13] Therefore, at room temperature (RT), the dominant charge carriers in 3D materials are free electrons and holes. In contrast, in many 2D materials, the majority of charge carriers are usually excitons at RT, the tighter association of electrons and holes caused by exciton

H. Yao, Z. Li, Y. Xu, Q. Wang, G. Peng, Y. Lei, Z. Ci, Z. Jin
School of Materials and Energy & School of Physical Science
and Technology & Key Laboratory for Magnetism and Magnetic
Materials of the Ministry of Education
Lanzhou University
Lanzhou 730000, P. R. China
E-mail: cizhp@lzu.edu.cn; jinzw@lzu.edu.cn
C. Shi
School of College of Chemistry and Chemical Engineering
Lanzhou University
Lanzhou 730000, P. R. China

Z. H. Li
School of Physical Science and Technology & Lanzhou
Center for Theoretical Physics & Key Laboratory of Theoretical
Physics of Gansu Province
Lanzhou University
Lanzhou 730000, P. R. China
E-mail: lizhenhua@lzu.edu.cn
H. Wang
Delft University of Technology
Photovoltaic Materials and Devices Group
Mekelweg 4, Delft 2628 CD, The Netherlands

ADVANCED
SCIENCE NEWS
www.advancedsciencenews.com

ADVANCED
FUNCTIONAL
MATERIALS
www.afm-journal.de

binding inhibits efficient charge separation and transport.[14,15] 2) Due to the unique natural multiple quantum well structures of 2D perovskite, charge transport between inorganic layers is regarded as an organic interlayer-mediated tunneling process, and barrier width and height of quantum well determine the tunneling probability.[16–18] The former can be tuned by the size of the spacer cations, and the latter depends on the energy alignment between the inorganic and organic layers, and the degree of intermolecular electronic coupling between adjacent organic cations.[19,20]

To date, most of the reported organic spacers of 2D CsPbI$_3$ perovskites are single-ring aromatic or aliphatic spacers, such as phenethylammonium (PEA), 1,4-butanediammonium (BDA), and n-butylammonium (BA).[21–25] For these spacers, due to energy level mismatch and low electronic coupling, it is difficult to eliminate the barrier of charge tunneling through the organic interlayer, resulting in low carrier mobility. Meanwhile, these spacers generally have low dielectric constant and poor conductivity, which are adverse to efficient charge transport and optoelectronic properties. Therefore, there is an urgent need to develop more efficient organic spacers to enhance charge transport and gain insight into their charge separation and transport mechanisms.

Surprisingly, Passarelli et al. found that the naphthalene- and pyrene-based conjugated multiple-ring aromatic spacers have larger dielectric constant and more excellent conductivity.[26] Liu and his group confirmed that the extensive π-electron delocalization along the conjugated backbone not only can weaken the dielectric confinement by reducing the dielectric mismatch between the inorganic layer and the adjacent organic layer, but also improve the energy level matching between the inorganic layers and organic galleries, thereby improving the charge transport of photovoltaic devices.[27,28] In addition, its strong π–π conjugation can also promote the formation of 2D perovskites and improve the charge transport in the layered structure due to the strong interaction between functional groups of organic spacers.[29] However, in 2D CsPbI$_3$ PSCs, π-conjugated multiple-ring aromatic spacers remain largely unexplored for their influence on optoelectronic properties and instinct mechanisms.

In this work, a novel multiple-ring aromatic spacer, 1-naphthylamine (1-NA) for 2D RP CsPbI$_3$ perovskites is successfully developed and demonstrated to exhibit high photovoltaic performance. Compared with the conventional single-ring aromatic PEA spacer, the 1-NA spacer with extended π-conjugated length has a larger dipole moment, which reduces the exciton binding energy. Meanwhile, its π-electron contributes to the conduction band (CB), which can reduce the bandgap of the layered perovskite. In addition, it is further demonstrated that the strong NH···I hydrogen bonding interaction between the 1-NA organic spacer and the inorganic layer can induce vertically oriented growth to prepare perovskite films with low density of defect states and improved charge transport, and obtain a record PCE of 16.62%.

2. Results and Discussion

Here, relative to the PEA spacer, the 1-NA spacer was ingeniously designed, and corresponding 2D (PEA)$_2$Cs$_{n-1}$Pb$_n$I$_{3n+1}$ and (1-NA)$_2$Cs$_{n-1}$Pb$_n$I$_{3n+1}$ perovskites were named PEA-Pb and 1-NA-Pb, respectively. First, theoretical simulations elucidate the advantages of the extended π-conjugation length of 1-NA spacer on the optoelectronic properties of 2D RP CsPbI$_3$ perovskites. The density functional theory calculations in **Figure 1**a and Figure S1, Supporting Information depict that the dipole moments of the 1-NA and PEA molecules are 1.81 and 1.24 D, respectively. The high polarity of the 1-NA molecules can increase its dielectric constant, leading to reduction in the dielectric mismatch between the organic layer and the adjacent inorganic layer, reducing the 2D perovskite exciton binding energy. Thereby, the Coulomb force between the electron and hole pairs of the excitons is reduced, promoting efficient charge separation.[30,31]

Figure 1b illustrates several possible carrier transport channels between the interlayers. H bond: the −NH$_3^+$ functional groups of PEA$^+$ and 1-NA$^+$ cations occupy the site of Cs$^+$ and connect the inorganic layer through NH···I hydrogen bonds. Pb–π coupling: due to the presence of benzene ring molecules, the layer interaction can also be increased through Pb–π coupling to improve charge transport.[32] I–I interaction: cations connect the corresponding inorganic layers through van der Waals forces and π–π conjugated interactions. Under different dimensions (n = 2, 3, 4), the NH···I distance of 1-NA-Pb is smaller than that of PEA-Pb, which indicates that the extended π-conjugation length of the 1-NA pacer can enhance H-bonds interactions (Figure S2a, Supporting Information). Meanwhile, the extended π-conjugation length results in stronger π–π conjugation and strong interaction between organic spacers. Besides, the chemical interaction between −NH$_3^+$ and terminal I$^-$ ions will generate a torque, which drives the rotation of the [PbI$_6$]$^{4-}$octahedron along with the rotation of the central Pb cation, and the shorter NH···I distance can lead to larger structures distortion.[33] The equatorial (parallel to the inorganic plate) and axial (perpendicular to the inorganic plate) Pb-I-Pb and I-Pb-I bond angles can further illustrate the changes in structural distortion (Figure 1c and Figure S2b–e, Supporting Information).

Figure 1d,f presents the band gaps of PEA-Pb and 1-NA-Pb perovskites, respectively, which both exhibit direct bandgap and decrease with an increasing value of n. Notably, 1-NA-Pb perovskite exhibits bandgap of 1.7622, 1.6121, and 1.5615 eV for n = 2, 3, 4, respectively, which are smaller than those of PEA-Pb perovskite (1.83438, 1.7742, 1.7334 eV, for n = 2, 3, 4, respectively). Figure 1e,g is the density of states (DOS) of PEA-Pb and 1-NA-Pb perovskites based on n = 4, respectively. For PEA-Pb perovskite, the valence band maximum (VBM) mainly originates from the p orbitals of I ions and a small fraction of the s orbitals of the Pb ions, whereas the conduction band minimum (CBM) is mainly from the p orbitals of Pb ions. Differently, the CBM of 1-NA–Pb perovskite is mainly contributed by Org (organic spacer) p orbitals and a small fraction of Pb p orbitals, suggesting that its 1-NA cation contributes significantly to the CB, which is consistent with the reported conjugated aromatic 2,2-biimidazolium (BIDZ) and N,N-dimethylphenylene-p-diammonium (DPDA) cations.[34] Unlike the conventional VBM and CBM of most 2D perovskite materials located on the inorganic layer, the π-electrons in 1-NA, BIDZ, and DPDA molecules have a significant contribution to CBM, which can lead
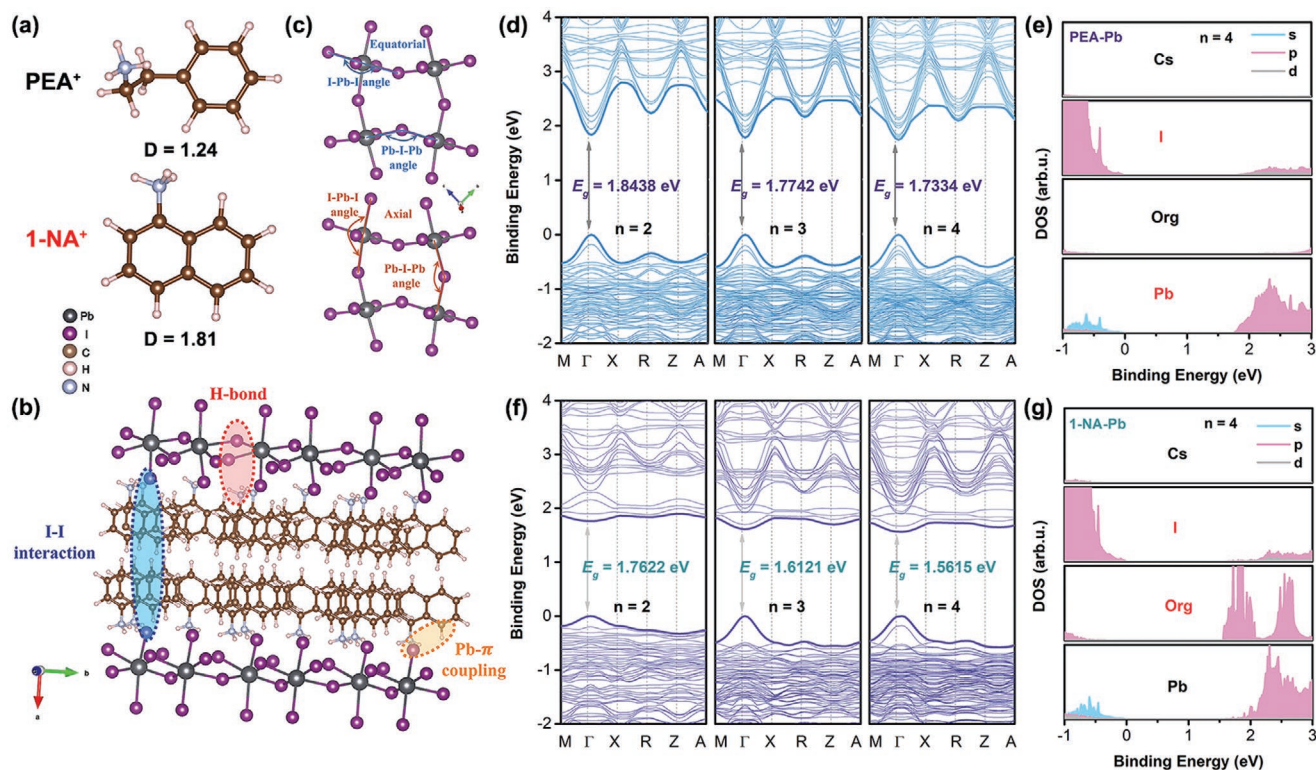
Figure 1. Structural simulation data of PEA+ and 1-NA+ spacer and the corresponding 2D perovskites: a) Molecular structures and calculated molecular dipole moments of PEA+ and 1-NA+ spacer; b) schematic diagram of the three carrier transport channels between the interlayers; c) definition of equatorial and apical Pb-I-Pb and I-Pb-I angles; calculated band structures of d) PEA-Pb perovskite ($n = 2$, 3, and 4) and f) 1-NA-Pb perovskite ($n = 2$, 3, and 4), VBM is set to zero; DOS of s, p and d orbitals of Cs, I, organic (Org) and Pb ions in e) PEA-Pb perovskite ($n = 4$) and g) 1-NA-Pb perovskite ($n = 4$).

to a reduced bandgap of layered perovskites, and promote the absorption of photons by the perovskite to generate more electron-hole pairs and facilitate charge transport. Meanwhile, we speculate that the π and π^* states located in the near-edge CB can also facilitate the electronic coupling between the organic layers and the inorganic layers, optimizing the mobility of carriers and more favorable photovoltaic performance, which is consistent with that reported by Xiao et al.[35] This is also proved by the DOS result under other dimensions ($n = 2$, 3) (Figure S3a–d, Supporting Information).

Benefiting from the advantages of the 1-NA spacer, we fabricated 2D ($n = 4$) RP 1-NA-Pb and PEA-Pb perovskite films by one-step spin coating using methylammonium chloride (MACl) in isopropanol (IPA) solution as an anti-solvent to induce crystal growth.[36–39] To explore whether NH···I hydrogen bonding interactions exist between the PEA+/1-NA+ cations and the inorganic layer, a series of characterizations were performed. **Figure 2**a displays the Fourier transform infrared (FTIR) spectra of PEA-Pb and 1-NA-Pb powder scraped from glass substrate. From its enlarged view, the N-H stretching vibration of 1-NA-Pb shifts to lower wavenumbers (3448–3440 cm^{-1}) relative to PEA-Pb, and this apparent transition indicates the occurrence of NH···I hydrogen bonding interactions.[25,40] The H nuclear magnetic resonance (1H NMR) is used to check the structure of PEAI and 1-NAI in Figure S4, Supporting Information, and the integrated areas of both are well corresponding to their structures. Moreover, Figure 2b lists that the −NH$_3^+$

signals of PEA-Pb and 1-NA-Pb appear at 8.26 and 8.11 ppm, respectively, exhibiting a distinct chemical shift relative to the −NH$_3^+$ signals of PEAI and 1-NAI, which further demonstrated the existence of NH···I hydrogen bond interaction.[28]

The X-ray photoelectron spectroscopy (XPS) further verified the strong NH···I hydrogen bonding interaction (Figure 2c–f). For the PEA-Pb film, two main peaks at 134.6 and 139.4 eV are Pb 4f$_{7/2}$ and Pb 4f$_{5/2}$, and two main peaks at 615.5 and 627.0 eV are I 3d$_{5/2}$ and I 3d$_{3/2}$, and two main peaks at 721.0 and 735.0 eV are Cs 3d$_{5/2}$ and Cs 3d$_{3/2}$. The characteristic peaks in the XPS spectrum of the 1-NA-Pb film were significantly shifted to lower values (≈0.2 eV) compared to the PEA-Pb film. This suggests that the presence of strong NH···I hydrogen bonding between the 1-NA cation and [PbI$_6$]$^{4-}$ interaction, resulting in change for the chemical bond length of Pb-I in [PbI$_6$]$^{4-}$ octahedron, which is the same as previous reports and also in good agreement with the data in simulation.[27,41] Ultraviolet photoelectron spectroscopy emission spectroscopy in Figure 2g was used to reveal the energy level changes of PEA-Pb and 1-NA-Pb perovskite. Combined with the bandgaps obtained from the simulations, the valence band (VB) and CB positions of the samples were determined, and the corresponding calculated results are plotted in Figure 2h. Compared with PEA-Pb perovskite, 1-NA-Pb perovskite can better match with the TiO$_2$ and Spiro-OMeTAD energy levels, thereby facilitating charge transport and extraction.

Scanning electron microscopy (SEM), atomic force microscopy (AFM), and contact angle were used to investigate the

**ADVANCED
SCIENCE NEWS**

www.advancedsciencenews.com

**ADVANCED
FUNCTIONAL
MATERIALS**

www.afm-journal.de
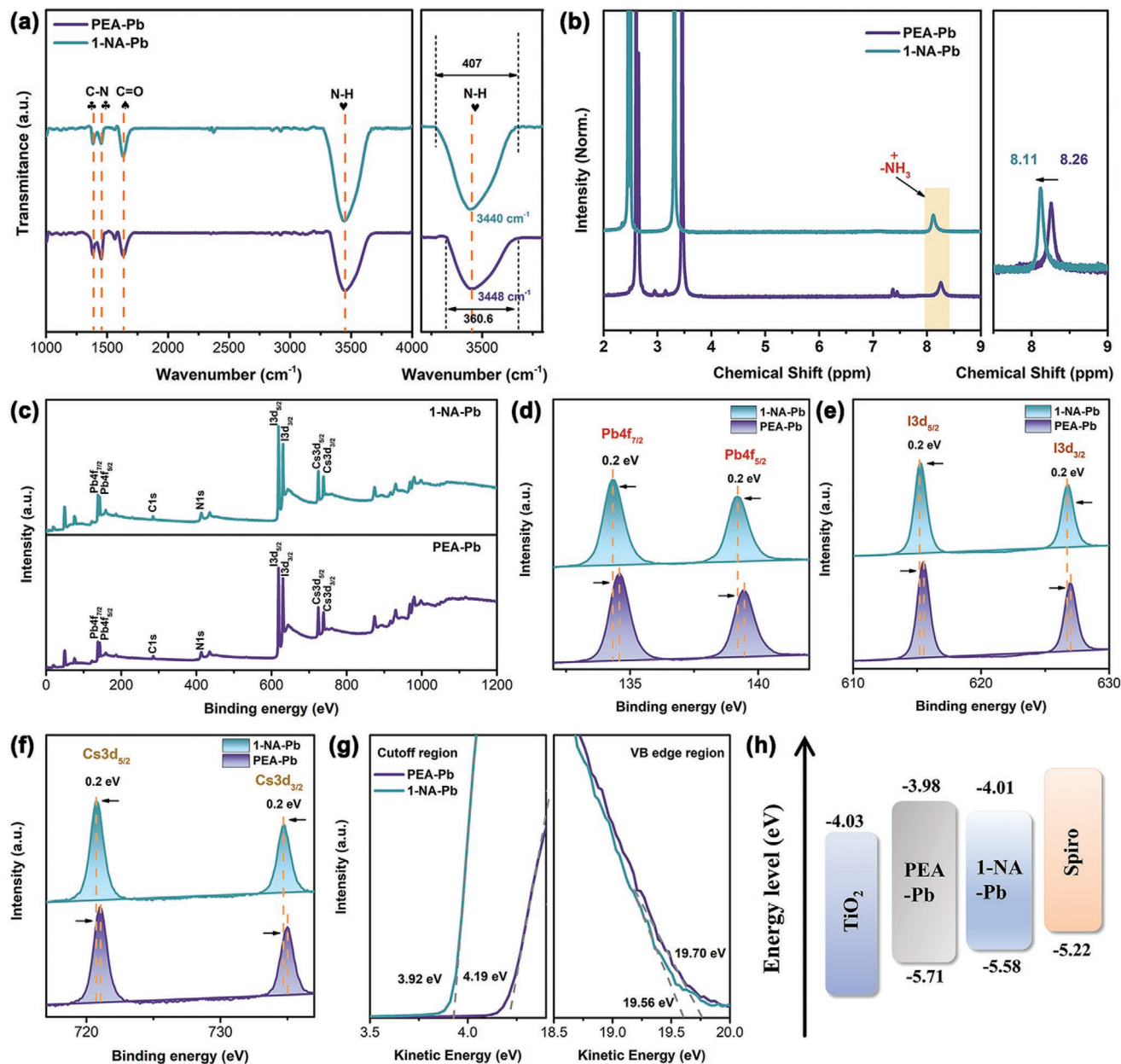
Figure 2. Interaction and band analysis of PEA-Pb and 1-NA-Pb perovskites ($n = 4$): a) FTIR spectra and enlarged FTIR spectra; b) ^{1}H NMR spectra and enlarged ^{1}H NMR spectra showing changes in the resonance signals generated from the H protons; c) XPS spectra; high-resolution XPS spectra: d) Pb 4f; e) I 3d; f) Cs 3d; g) UPS spectra of the cut-off region (left) and VB edge region (right); h) schematic diagram of the energy band structure.

effect of 1-NA spacer on film morphology and wettability. **Figure 3**a,b are SEM and AFM images of the PEA-Pb film, showing poor film quality with obvious pinholes and relatively large root-mean-square (RMS) roughness of 31.7 nm, which is not conducive to the contact of perovskite layer and transport layer resulted in cause significant leakage current. Comparatively, the morphology of 1-NA-Pb film is significantly improved, becoming denser and more uniform with smaller RMS roughness of 22.8 nm, which is beneficial to suppress the recombination of carriers and reduce the nonradiative loss (Figure 3c,d).[42] Due to the improved film quality, the contact

angle of the 1-NA-Pb film was increased from 80.54° to 90.05° relative to the PEA-Pb film, indicating improved moisture resistance. Further, we evaluated the effect of MACl additives on the morphology of PEA-Pb and 1-NA-Pb films, whose corresponding SEM are illustrated in Figures S5 and 6, Supporting Information. The homogeneity and compactness of PEA-Pb and 1-NA-Pb-based films were improved with increasing MACl additive concentration, and the optimal concentration was both 4 mg mL^{-1}. To reveal the effect of 1-NA spacer on film crystallization, the crystallization process of the corresponding film annealing was tested (Figure S7, Supporting Information). The
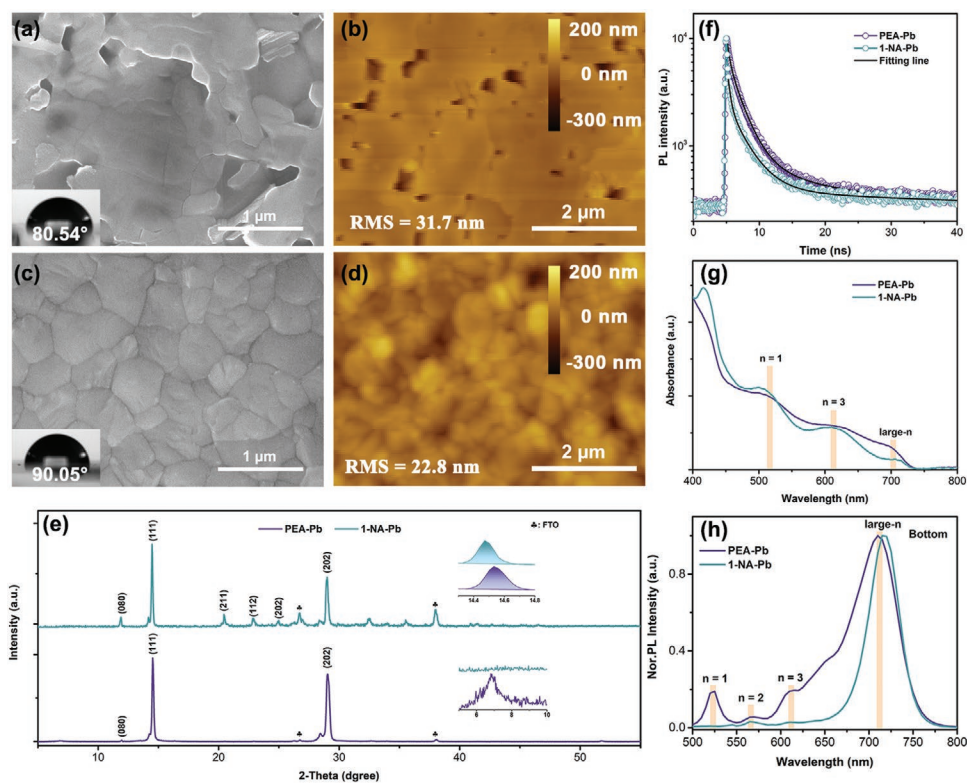
Figure 3. Surface and optical characterization of the PEA-Pb and 1-NA-Pb film ($n = 4$): SEM (insert: contact angle image of perovskite film underwater) and AFM of a,b) PEA-Pb film and c,d) 1-NA-Pb film; e) XRD patterns; f) TRPL spectra of film deposited on glass/TiO₂; g) UV-Vis absorption spectra; h) PL spectra excited from glass substrate side (bottom side).

1-NA-Pb film shows a faster crystallization rate than the PEA-Pb film in the early stages of annealing process, which may be attributed to the enhanced NH···I hydrogen bonding interactions analyzed above. In addition, we speculate that strong $\pi–\pi$ conjugation can also lead to enhanced intermolecular interactions in 1-NA-Pb, thereby promoting the formation of 2D perovskite films with preferential crystal growth and optimized film quality.[28,29]

The effect of the 1-NA spacer on the crystal orientation of 2D RP CsPbI₃ perovskite film was further explored by X-ray diffraction (XRD). Two diffraction peaks of the (111) and (202) planes for PEA-Pb film are displayed around 14.5° and 29.0°, as indicated in Figure 3e. For the 1-NA-Pb film, the corresponding peaks shifts to a lower angle, and the decrease in 2θ angle indicates lattice expansion in the 1-NA-Pb film, which may be due to the extended π-conjugation length of 1-NA spacer.[43] A distinct peak attributable to (0k0) diffraction is observed in the PEA-Pb film at around 6.8°, which indicates that a small fraction of layered corner-sharing [PbI₆]⁴ sheets parallel to the substrate.[28] However, no (0k0) diffraction peak was observed for the 1-NA-Pb film below 10°, indicating that the 1-NA-Pb perovskite has a vertical orientation, which facilitates charge transport between the transport layers.[44] Considering the unique structure of 1-NA spacer, the better crystal orientation is attributed to the strong molecular interaction of spacers, which can form an ordered crystal structure and induce crystal growth.[45] Figure 3f plots the time-resolved photoluminescence curves with a structure of glass/TiO₂ or 1-NA-Pb film, and the

calculated carrier lifetimes are listed in Table S1, Supporting Information. Compared with PEA-Pb films, its carrier lifetime is shortened in 1-NA-Pb films, which can be attributed to the superior crystallinity of 1-NA-Pb film and energy level matching with the TiO₂ layer, reducing nonradiative recombination and facilitating electron extraction.[46,47]

The ultraviolet-visible (UV-vis) absorption spectra are illustrated in Figure 3g. PEA-Pb and 1-NA-Pb films have several distinct exciton peaks around 515, 615, and 705 nm, representing $n = 1$, 3, and large-n phases ($n \approx \infty$), respectively, indicating that there are multiple perovskite phases with different n values in the perovskite film.[48] Steady-state photoluminescence (PL) excited from the bottom and front side was further carried out to explore the role of 1-NA spacer on the phase distribution in 2D RP CsPbI₃ film. Figure 3h exhibits PL excited from the bottom side, for PEA-Pb film, distinct exciton emission peaks are observed at 515, 570, 615, and 705 nm, corresponding to $n = 1$, 2, 3, and large-n phases. In general, the $n = 1$ phase easily stacks along the direction parallel to substrate, which is not conducive to efficient charge transport in PSCs.[49,50] Differently, in the 1-NA-Pb film, $n = 2$, 3 and large-n phases dominate, and the corresponding exciton peaks are concentrated around 570, 615, and 705 nm. The absence of $n = 1$ phase will improve efficient charge transport, and the 1-NA-Pb film is more prone to vertical orientation growth, which is consistent with the XRD data. Figure S8a, Supporting Information gives PL spectra excited from the front side, both films have only the large-n phase. The difference between the top and bottom PL spectra indicates that
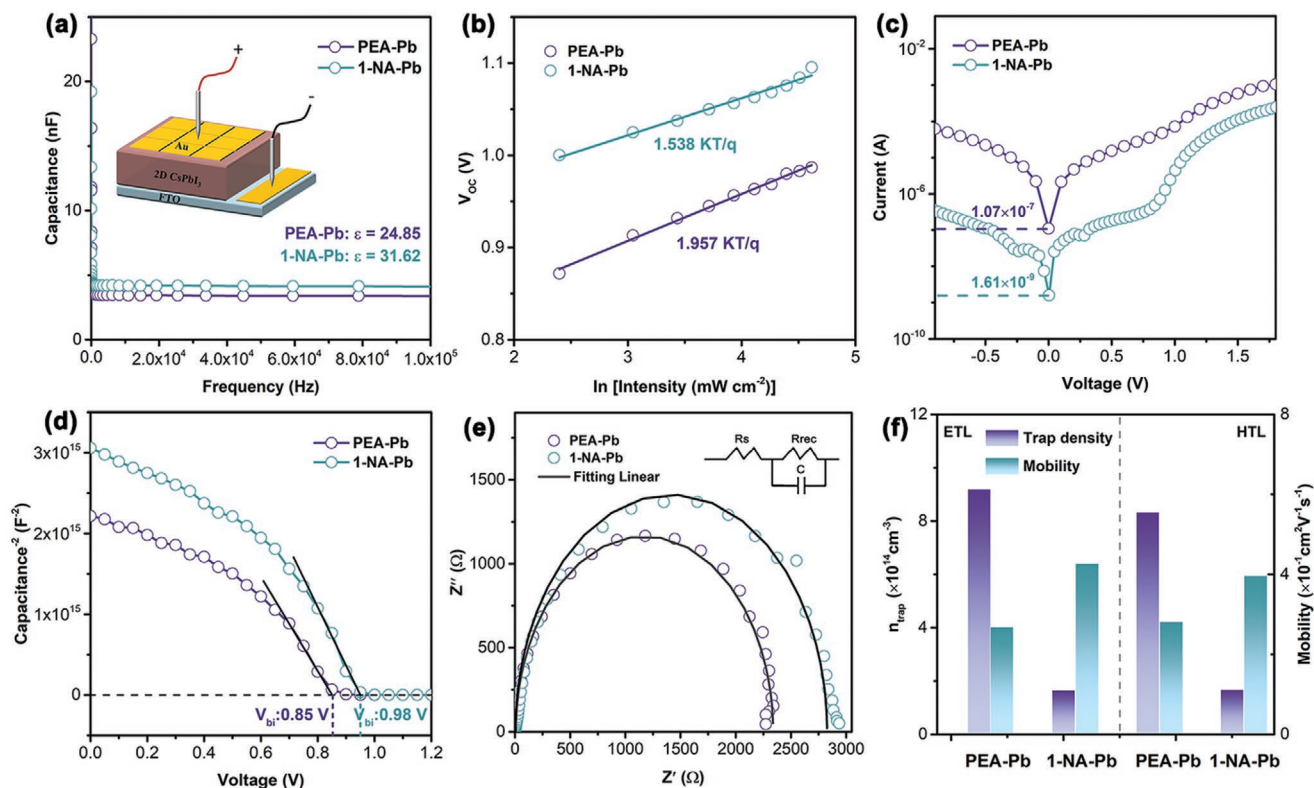
Figure 4. Optoelectronic characterization of the PEA-Pb and 1-NA-Pb based devices ($n = 4$): a) Capacitance versus frequency at room temperature for PEA-Pb and 1-NA-Pb; b) V_{OC} versus light intensity; c) dark J–V curves; d) Mott–Schottky curves; e) EIS data; f) Carrier mobility and trap density comparison of electron-only and hole-only PSCs.

an ordered gradient phase distribution is formed in PEA-Pb and 1-NA-Pb films.[51]

Next, the dielectric constant (ε) of the material was measured and calculated from the frequency-dependent capacitance curve in **Figure** 4a, the ε of 1-NA-Pb was 31.62, which was greater than that of PEA-Pb (24.85), which further confirms that the high polarity of 1-NA molecules in theoretical analysis changes the surrounding dielectric environment and increases the dielectric constant of the material.[28] The thickness of the perovskite active layer film used here is about 600 nm, which is obtained by measuring its cross-section SEM (Figure S8b, Supporting Information). The charge carrier recombination loss in PEA-Pb and 1-NA-Pb devices were explored using light intensity (I)-dependent current density–voltage (J–V) characteristics. Figure 4b plots the linear fit of open-circuit voltage (V_{OC}) to the logarithm of I. Compared with the PEA-Pb device, the ideality factor of the 1-NA-Pb device is reduced from 1.957 to 1.538 kT q^{-1}. The lower ideality factor indicates reduced trap-assisted recombination, which is attributed to the enhanced crystallinity and improved film quality of the 1-NA-Pb film.[52] Short-circuit current density (J_{SC}) and I exhibited linear relationship in a double logarithmic scale ($J \propto I^{\alpha}$) (Figure S8c, Supporting Information), and the α value (1.017) of the 1-NA-Pb-based device was closer to 1 than that of PEA-Pb (1.088), indicating that its bimolecular recombination is lower due to the reduction of defects.[53] The dark J–V curves of PEA-Pb and 1-NA-Pb devices are presented in Figure 4c. It is evident that the 1-NA-Pb device

provides a smaller dark J_{SC}, which indicates that the extended π-conjugation length of 1-NA spacers can repair defects and traps in perovskite film, thereby reducing leakage current.[54] In addition, the capacitance–voltage (C–V) curves further explore carrier extraction and transport, with a built-in potential (V_{bi}) of 0.85 V for PEA-Pb devices and 0.98 V for 1-NA-Pb devices. The increased V_{bi} plays a role in enhancing the separation of photo-generated carriers, which can lead to more efficient charge transfer (Figure 4d).[55] Electrochemical impedance spectroscopy was tested under dark conditions, and its Nyquist plot is exhibited in Figure 4e. The 1-NA-Pb device has a larger recombination resistance (R_{rec}), indicating that charge recombination based on this system is suppressed.

In order to further explore the defect states and carrier situations of different systems, the Space-Charge-Limited-Current (SCLC) was measured under dark conditions (Figure S9 a–d, Supporting Information). The calculated charge carrier mobility (μ) and trap density (n_{trap}) of PEA-Pb and 1-NA-Pb devices are counted in Figure 4f, and the corresponding results are summarized in Table S2, Supporting Information. The μ of the 1-NA-Pb device is larger than that of the PEA-Pb device, regardless of whether it is an electron or hole type device, which may be attributed to the preferential vertical orientation and the matching energy levels of 1-NA-Pb film, resulting in increased hole and electron mobility. The lower n_{trap} further confirms that due to the improved quality of 1-NA-Pb film, the reduced charge carrier recombination favors charge transport.[56–58]
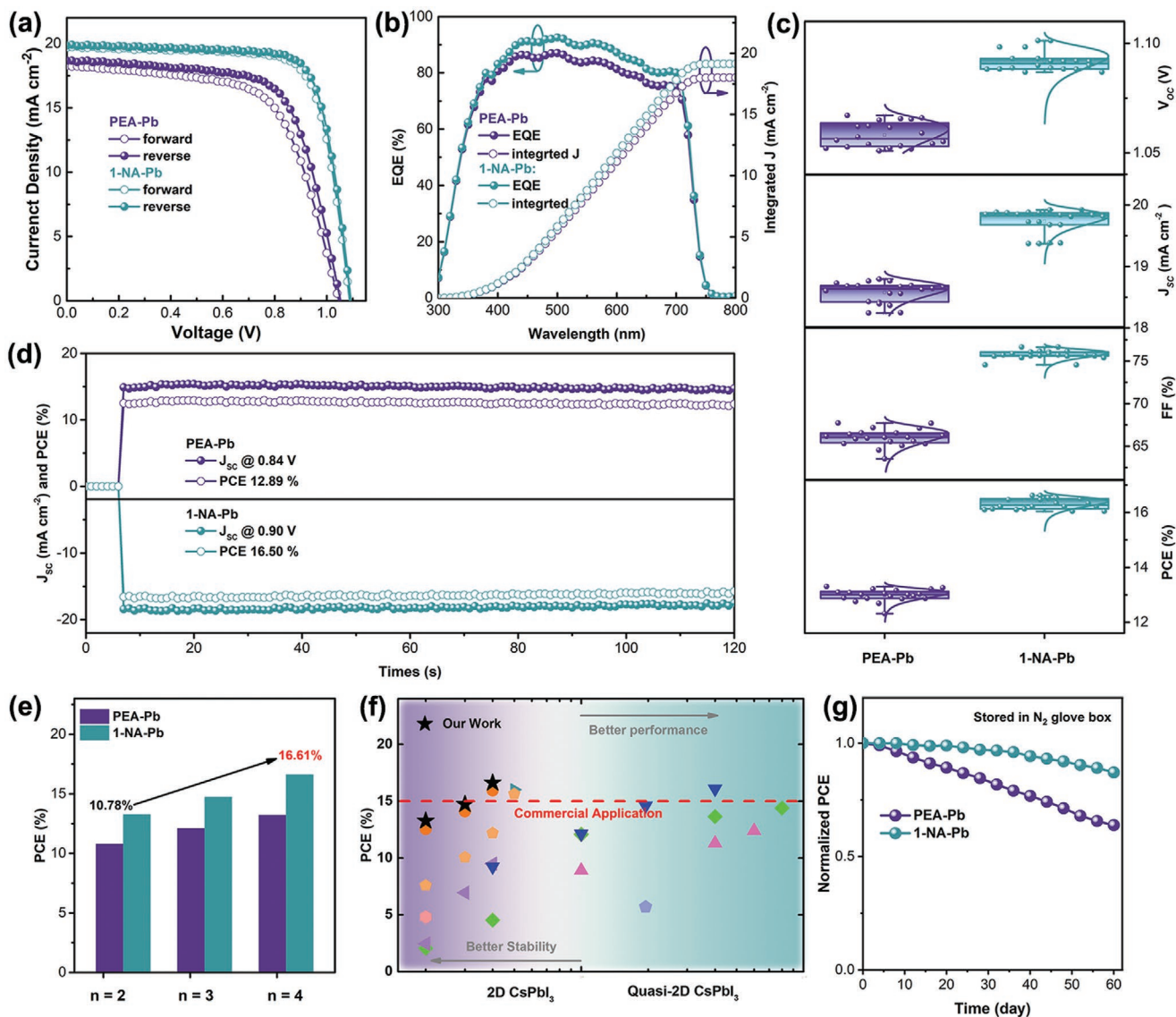
Figure 5. Device performance of the PEA-Pb and 1-NA-Pb PSCs ($n = 4$): a) J–V characteristics in forward and reverse scan with an area of 0.09 cm^2; b) EQE and the integrated product of the EQE curves; c) statistical distribution of different photovoltaic parameters (V_{OC}, J_{SC}, FF, and PCE) under 20 devices; d) stable measurement at the maximum power point under continuous AM 1.5G illumination; e) PCE increase in different n values ($n = 2, 3$, and 4); f) PCE distribution of 2D or quasi-2D CsPbI$_3$ PSCs **in** different dimensions relative to reported work; g) long-term stability of the unencapsulated PEA-Pb and 1-NA-Pb devices under N$_2$-filled glovebox for 60 days.

Photovoltaic devices were fabricated via the structure of FTO/TiO$_2$/2D RP CsPbI$_3$/Spiro-OMeTAD/MoO$_3$/Ag. By using PEA-Pb and 1-NA-Pb ($n = 4$) perovskites as photoactive layers, the corresponding J–V characteristic curves are illustrated in **Figure 5**a and the performance parameters are listed in **Table 1**. The PEA-Pb device has a lower PCE (13.20%), V_{OC} (1.053 V), J_{SC} (18.67 mA cm^{-2}), and fill factor (FF) (67.17%). After using the extended π-conjugated spacer, the V_{OC} of 1-NA-Pb device was significantly increased to 1.093 V, J_{SC} to 19.84 mA cm^{-2}, FF to 76.63%, and PCE to 16.62%.[7,48,59] The improved performance of 1-NA-Pb devices is attributed to the enhancement of overall photovoltaic parameters, which benefit from the improved quality of discussed 1-NA-Pb films, the preferred vertical crystal orientation, the reduced defect density, and the lower binding

energy of layered perovskites due to the larger dipole moments of 1-NA molecules (Figure S10 and Table S3–S4, Supporting Information). Figure 5b depicts the external quantum efficiency

Table 1. The photovoltaic parameters of the PEA-Pb ($n = 4$) and 1-NA-Pb ($n = 4$) PSCs under both reverse and forward scan directions. (Extracted from Figure 5a).

Device	Scan mode	J_{SC} (mA cm^{-2})	V_{OC} [V]	FF [%]	PCE [%]
PEA-Pb	Reverse	18.67	1.053	67.17	13.20
	Forward	18.29	1.047	63.00	12.06
1-NA-Pb	Reverse	19.84	1.093	76.63	16.62
	Forward	19.68	1.088	75.70	16.21

Table 2. The photovoltaic parameters of the PEA-Pb and 1-NA-Pb PSCs in different n values ($n = 2$, 3, and 4) under reverse scan directions. (Under 20 devices, extracted from Figure 5e).

n value	Device	J_{SC} [mA cm^{-2}]	V_{OC} [V]	FF [%]	PCE [%]	PCE$_{max}$ [%]
$n = 4$	PEA-Pb	19.47 ± 0.43	1.057 ± 0.010	66.01 ± 2.50	12.87 ± 0.33	13.20
	1-NA-Pb	19.73 ± 0.36	1.091 ± 0.009	75.72 ± 1.17	16.31 ± 0.30	16.62
$n = 3$	PEA-Pb	18.34 ± 0.54	1.032 ± 0.016	60.51 ± 3.76	11.70 ± 0.39	12.09
	1-NA-Pb	19.28 ± 0.29	1.043 ± 0.014	71.12 ± 2.26	14.47 ± 0.26	14.73
$n = 2$	PEA-Pb	17.17 ± 0.36	1.019 ± 0.039	59.04 ± 1.94	10.42 ± 0.36	10.78
	1-NA-Pb	18.61 ± 0.14	1.024 ± 0.030	67.96 ± 0.86	12.95 ± 0.31	13.26

spectra of PEA-Pb and 1-NA-Pb PSCs at a wavelength of 300–800 nm, where the 1-NA-Pb PSCs exhibit enhanced spectral responses relative to the PEA-Pb PSCs.[60] Under AM 1.5G illumination condition, the integrated J_{SC} of PEA-Pb and 1-NA-Pb were 18.01 and 19.13 mA cm^{-2}, respectively. Next, based on PEA-Pb and 1-NA-Pb PSCs, the distributions of photovoltaic parameters (V_{OC}, FF, J_{SC}, and PCE) for 20 individual devices were counted (Figure 5c), indicating good reproducibility. Figure 5d shows the steady-state photocurrent and PCE measurements test. Both PEA-Pb and 1-NA-Pb PSCs show 15.35 mA cm^{-2} (18.34 mA cm^{-2}) steady-state photocurrent and stable PCE 12.89% (16.50%).

Benefiting from the advantage of extended π-conjugation length in the 1-NA spacer, Figure 5e exhibits that the performance of 1-NA-Pb PSCs is greatly improved relative to the PEA-Pb PSCs under different dimensions ($n = 2$, 3, 4). Its specific J-V curve and photovoltaic parameter statistics are shown in Figure S11, Supporting Information and **Table 2**. Next, Figure 5f compares this result with the PCE of 2D/quasi-2D CsPbI$_3$ PSCs that have been reported so far in different dimensions, and Table S5, Supporting Information summarizes the corresponding photovoltaic parameters.[1,7,21–25,48,59] The 1-NA-Pb PSCs achieved record-breaking performance in 2D PSCs, meeting the needs of commercial applications. Figure 5g counts the changes in the performance of PEA-Pb and 1-NA-Pb devices in nitrogen (N$_2$) atmosphere to check the long-term stability of devices. The unencapsulated 1-NA-Pb device retained 87.1% of the initial PCE after 60 days of storage, while the PEA-Pb device dropped to 63.8% under the same conditions. In addition, Figure S12, Supporting Information also tested the stability of PEA-Pb and 1-NA-Pb films and devices under heating and humidity environments. Compared with PEA-Pb, 1-NA-Pb has better stability in any case. This indicates that the 1-NA-Pb devices show more stable properties than PEA-Pb devices. The improved stability is due to intrinsic structural stability of 2D RP perovskites with extended π-conjugated length aromatic spacers. Overall, the preferred vertical crystal orientation, reduced defect state density, and excellent water resistance are responsible for the outstanding photovoltaic performance and excellent stability of 1-NA-Pb films and devices.

3. Conclusion

In conclusion, an aromatic spacer 1-NA with extended π-conjugation length was successfully designed for 2D RP CsPbI$_3$ perovskites. The 1-NA spacer in 1-NA-Pb perovskite

can reduce the dielectric mismatch between the organic layer and the adjacent inorganic layer, so the exciton binding energy of the 1-NA-Pb system is smaller, reducing the possibility of undesired carrier recombination before reaching the extraction layer, which promotes charge separation. Meanwhile, its unique molecular structure not only can reduce the bandgap of 1-NA-Pb perovskite and promote the coupling of organic and inorganic layers, but also bring about stronger hydrogen bonds and organic intermolecular interactions, which helps to reduce the charge tunneling barrier through the organic interlayer and enhance the charge transport. Benefiting from the advantages of 1-NA spacer, the coverage, smoothness, and uniformity of 1-NA-Pb film were significantly improved with preferred vertical orientation compared to the PEA-Pb film. In addition, trap density and nonradiative recombination losses are greatly suppressed. Finally, 1-NA-Pb PSCs ($n = 4$) obtained a record PCE of 16.62%. In short, this work provides an efficient way to design spacers with extended π-conjugation lengths for 2D RP CsPbI$_3$ PSCs with excellent PCE and stability.

Supporting Information

Supporting Information is available from the Wiley Online Library or from the author.

Conflict of Interest

The authors declare no conflict of interest.

Authors Contribution

H.Y. Z.L., and C.S. performed the experiments, data analysis, and experimental planning. Z.H. Li conducted a theoretical simulation analysis. The project was conceived, planned, and supervised by Z.J. and Z.C. Some of the experimental tests was supported by Y.X. Y.L G.P. H.W.,

and Q.W. The manuscript was written by H.Y. All the authors reviewed the manuscript.

[1] Y. Jiang, J. Yuan, Y. Ni, J. Yang, Y. Wang, T. Jiu, M. Yuan, J. Chen, *Joule* **2018**, *2*, 1356.

[2] J. Liang, Z. Zhang, Q. Xue, Y. Zheng, X. Wu, Y. Huang, X. Wang, C. Qin, Z. Chen, C.-C. Chen, *Energy Environ. Sci.* **2022**, *15*, 296.

[3] Y. Xu, M. Wang, Y. Lei, Z. Ci, Z. Jin, *Adv. Energy Mater.* **2020**, *10*, 2002558.

[4] Z. Li, F. Zhou, H. Yao, Z. Ci, Z. Yang, Z. Jin, *Mater. Today* **2021**, *48*, 155.

[5] Y. Cheng, L. Ding, *SusMat* **2021**, *1*, 324.

[6] A. L. Rogach, *Light: Sci. Appl.* **2021**, *10*, 46.

[7] Z. Xu, L. Li, X. Dong, D. Lu, R. Wang, W.-J. Yin, Y. Liu, *Nano Lett.* **2022**, *22*, 2874.

[8] S. Tan, B. Yu, Y. Cui, F. Meng, C. Huang, Y. Li, Z. Chen, H. Wu, J. Shi, Y. Luo, D. Li, Q. Meng, *Angew. Chem., Int. Ed.* **2022**, *134*, e202201300.

[9] J. C. Blancon, A. V. Stier, H. Tsai, W. Nie, C. C. Stoumpos, B. Traoré, L. Pedesseau, M. Kepenekian, F. Katsutani, G. T. Noe, J. Kono, S. Tretiak, S. A. Crooker, C. Katan, M. G. Kanatzidis, J. J. Crochet, J. Even, A. D. Mohite, *Nat. Commun.* **2018**, *9*, 2254.

[10] L. M. Herz, *J. Phys. Chem. Lett.* **2018**, *9*, 6853.

[11] M. Baranowski, P. Plochocka, *Adv. Energy Mater.* **2020**, *10*, 1903659.

[12] H. Li, X. Wang, T. Zhang, X. Gong, Q. Sun, H. Pan, Y. Shen, S. Ahmad, M. Wang, *Adv. Funct. Mater.* **2019**, *29*, 1903293.

[13] S. Tan, N. Zhou, Y. Chen, L. Li, G. Liu, P. Liu, C. Zhu, J. Lu, W. Sun, Q. Chen, H. Zhou, *Adv. Energy Mater.* **2019**, *9*, 1803024.

[14] D. Marongiu, M. Saba, F. Quochi, A. Mura, G. Bongiovanni, *J. Mater. Chem. C* **2019**, *7*, 12006.

[15] D. B. Straus, C. R. Kagan, *J. Phys. Chem. Lett.* **2018**, *9*, 1434.

[16] A. Krishna, S. Gottis, M. K. Nazeeruddin, F. Sauvage, *Adv. Funct. Mater.* **2019**, *29*, 1806482.

[17] A. a. O. El-Ballouli, O. M. Bakr, O. F. Mohammed, *J. Phys. Chem. Lett.* **2020**, *11*, 5705.

[18] X. Zhu, Z. Xu, S. Zuo, J. Feng, Z. Wang, X. Zhang, K. Zhao, J. Zhang, H. Liu, S. Priya, S. F. Liu, D. Yang, *Energy Environ. Sci.* **2018**, *11*, 3349.

[19] Y. Gao, E. Shi, S. Deng, S. B. Shiring, J. M. Snaider, C. Liang, B. Yuan, R. Song, S. M. Janke, A. Liebman-Peláez, P. Yoo, M. Zeller, B. W. Boudouris, P. Liao, C. Zhu, V. Blum, Y. Yu, B. M. Savoie, L. Huang, L. Dou, *Nat. Chem.* **2019**, *11*, 1151.

[20] D. Sirbu, F. H. Balogun, R. L. Milot, P. Docampo, *Adv. Energy Mater.* **2021**, *11*, 2003877.

[21] J.-F. Liao, H.-S. Rao, B.-X. Chen, D.-B. Kuang, C.-Y. Su, *J. Mater. Chem. A* **2017**, *5*, 2066.

[22] F. Li, Y. Pei, F. Xiao, T. Zeng, Z. Yang, J. Xu, J. Sun, B. Peng, M. Liu, *Nanoscale* **2018**, *10*, 6318.

[23] K. Wang, Z. Li, F. Zhou, H. Wang, H. Bian, H. Zhang, Q. Wang, Z. Jin, L. Ding, S. Liu, *Adv. Energy Mater.* **2019**, *9*, 1902529.

[24] Z. Zhou, S. Yang, K. Xu, H. W. Qiao, J. Xie, Z. Lin, B. Ge, J. He, M. Chen, J. Zhang, Y. Hou, H. G. Yang, *J. Phys. Chem. Lett.* **2020**, *11*, 747.

[25] Z. Li, B. Ma, Y. Xu, Y. Lei, G. Peng, G. Wang, Q. Wang, H.-L. Zhang, Z. Jin, *Adv. Funct. Mater.* **2021**, *31*, 2106380.

[26] J. V. Passarelli, D. J. Fairfield, N. A. Sather, M. P. Hendricks, H. Sai, C. L. Stern, S. I. Stupp, *J. Am. Chem. Soc.* **2018**, *140*, 7313.

[27] Z. Xu, D. Lu, F. Liu, H. Lai, X. Wan, X. Zhang, Y. Liu, Y. Chen, *ACS Nano* **2020**, *14*, 4871.

[28] Z. Xu, D. Lu, X. Dong, M. Chen, Q. Fu, Y. Liu, *Adv. Mater.* **2021**, *33*, 2105083.

[29] B. Chaudhary, T. M. Koh, B. Febriansyah, A. Bruno, N. Mathews, S. G. Mhaisalkar, C. Soci, *Sci. Rep.* **2020**, *10*, 429.

[30] J. Shi, Y. Gao, X. Gao, Y. Zhang, J. Zhang, X. Jing, M. Shao, *Adv. Mater.* **2019**, *31*, 1901673.

[31] Q. Li, Y. Dong, G. Lv, T. Liu, D. Lu, N. Zheng, X. Dong, Z. Xu, Z. Xie, Y. Liu, *ACS Energy Lett.* **2021**, *6*, 2072.

[32] Z. Fang, X. Hou, Y. Zheng, Z. Yang, K.-C. Chou, G. Shao, M. Shang, W. Yang, T. Wu, *Adv. Funct. Mater.* **2021**, *31*, 2102330.

[33] Z. Fang, M. Shang, Y. Zheng, T. Zhang, Z. Du, G. Wang, X. Duan, K.-C. Chou, C.-H. Lin, W. Yang, X. Hou, T. Wu, *Mater. Horiz.* **2020**, *7*, 1042.

[34] M. P. Hautzinger, J. Dai, Y. Ji, Y. Fu, J. Chen, I. A. Guzei, J. C. Wright, Y. Li, S. Jin, *Inorg. Chem.* **2017**, *56*, 14991.

[35] Y. Lao, S. Yang, W. Yu, H. Guo, Y. Zou, Z. Chen, L. Xiao, *Adv. Sci.* **2022**, *9*, 2105307.

[36] T. Luo, Y. Zhang, Z. Xu, T. Niu, J. Wen, J. Lu, S. Jin, S. Liu, K. Zhao, *Adv. Mater.* **2019**, *31*, 1903848.

[37] Y. Zhang, J. Wen, Z. Xu, D. Liu, T. Yang, T. Niu, T. Luo, J. Lu, J. Fang, X. Chang, S. Jin, K. Zhao, S. Liu, *Adv. Sci.* **2021**, *8*, 2001433.

[38] H. Yao, S. Shi, Z. Li, Z. Ci, G. Zhu, L. Ding, Z. Jin, *J. Energy Chem.* **2021**, *57*, 567.

[39] S. Shan, Y. Li, H. Wu, T. Chen, B. Niu, Y. Zhang, D. Wang, C. Kan, X. Yu, L. Zuo, H. Chen, *SusMat* **2021**, *1*, 537.

[40] H. Bian, H. Wang, Z. Li, F. Zhou, Y. Xu, H. Zhang, Q. Wang, L. Ding, S. Liu, Z. Jin, *Adv. Sci.* **2020**, *7*, 1902868.

[41] C. Liu, R. Liu, Z. Bi, Y. Yu, G. Xu, H. Hou, Q. Wu, H. Yu, X. Xu, *Sol. RRL* **2021**, *5*, 2100495.

[42] W. Zhu, W. Chai, D. Chen, J. Ma, D. Chen, H. Xi, J. Zhang, C. Zhang, Y. Hao, *ACS Energy Lett.* **2021**, *6*, 1500.

[43] Y. Yan, S. Yu, A. Honarfar, T. Pullerits, K. Zheng, Z. Liang, *Adv. Sci.* **2019**, *6*, 1900548.

[44] F. Li, Y. Xie, Y. Hu, M. Long, Y. Zhang, J. Xu, M. Qin, X. Lu, M. Liu, *ACS Energy Lett.* **2020**, *5*, 1422.

[45] H. Ren, S. Yu, L. Chao, Y. Xia, Y. Sun, S. Zuo, F. Li, T. Niu, Y. Yang, H. Ju, B. Li, H. Du, X. Gao, J. Zhang, J. Wang, L. Zhang, Y. Chen, W. Huang, *Nat. Photonics* **2020**, *14*, 154.

[46] D. Bai, J. Zhang, Z. Jin, H. Bian, K. Wang, H. Wang, L. Liang, Q. Wang, S. F. Liu, *ACS Energy Lett.* **2018**, *3*, 970.

[47] D. Giovanni, M. Righetto, Q. Zhang, J. W. M. Lim, S. Ramesh, T. C. Sum, *Light: Sci. Appl.* **2021**, *10*, 2.

[48] H. Yao, G. Peng, Z. Li, Q. Wang, Y. Xu, B. Ma, Y. Lei, G. Wang, Q. Wang, Z. Ci, H.-L. Zhang, Z. Jin, *Nano Energy* **2022**, *92*, 106790.

[49] D. H. Cao, C. C. Stoumpos, O. K. Farha, J. T. Hupp, M. G. Kanatzidis, *J. Am. Chem. Soc.* **2015**, *137*, 7843.

[50] R. Quintero-Bermudez, A. Gold-Parker, A. H. Proppe, R. Munir, Z. Yang, S. O. Kelley, A. Amassian, M. F. Toney, E. H. Sargent, *Nat. Mater.* **2018**, *17*, 900.

[51] Z. Wang, Q. Wei, X. Liu, L. Liu, X. Tang, J. Guo, S. Ren, G. Xing, D. Zhao, Y. Zheng, *Adv. Funct. Mater.* **2021**, *31*, 2008404.

**ADVANCED
SCIENCE NEWS**

www.advancedsciencenews.com

**ADVANCED
FUNCTIONAL
MATERIALS**

www.afm-journal.de

[52] Y. Chen, J. Hu, Z. Xu, Z. Jiang, S. Chen, B. Xu, X. Xiao, X. Liu, K. Forberich, C. J. Brabec, Y. Mai, F. Guo, *Adv. Funct. Mater.* **2022**, *32*, 2112146.

[53] T. Singh, T. Miyasaka, *Adv. Energy Mater.* **2018**, *8*, 1700677.

[54] X. Wang, Y. Wang, Y. Chen, X. Liu, Y. Zhao, *Adv. Mater.* **2021**, *33*, 2103688.

[55] J. He, J. Su, Z. Lin, J. Ma, L. Zhou, S. Zhang, S. Liu, J. Chang, Y. Hao, *Adv. Sci.* **2021**, *8*, 2101367.

[56] J. He, H. Liu, F. Zhang, X. Li, S. Wang, *Adv. Funct. Mater.* **2022**, *32*, 2110030.

[57] Y. Lei, Z. Li, H. Wang, Q. Wang, G. Peng, Y. Xu, H. Zhang, G. Wang, L. Ding, Z. Jin, *Sci. Bull.* **2022**, https://doi.org/10.1016/j.scib.2022.05.019.

[58] J. Yao, Q. Chen, C. Zhang, Z. G. Zhang, Y. Li, *SusMat* **2022**, https://doi.org/10.1002/sus2.50.

[59] Z. Li, S. Yang, C. Ye, G. Wang, B. Ma, H. Yao, Q. Wang, G. Peng, Q. Wang, H.-L. Zhang, Z. Jin, *Small* **2022**, *18*, 2108090.

[60] C.-H. Kang, I. Dursun, G. Liu, L. Sinatra, X. Sun, M. Kong, J. Pan, P. Maity, E.-N. Ooi, T. K. Ng, O. F. Mohammed, O. M. Bakr, B. S. Ooi, *Light: Sci. Appl.* **2019**, *8*, 94.